RSC Advances

ROYAL SOCIETY
OF **CHEMISTRY**

www.rsc.org/advances

Microwave-Assisted Synthesis of Hematite/Activated Graphene Composites with Superior Performance for Photocatalytic Reduction of Cr(VI)

Yuanxin Du, [a] Zhuchen Tao, [a] Jian Guan, [a] Zijun Sun, [a] Wencong Zeng, [a] Pengchao Wen, [a] Kun Ni, [a] Jianglin Ye, [a] Shangfeng Yang, [a] Pingwu Du [a,b] and Yanwu Zhu [a,b,*]

[a] Key Laboratory of Materials for Energy Conversion, Chinese Academy of Sciences, Department of Materials Science and Engineering, University of Science and Technology of China, 96 Jin Zhai Rd, Hefei, Anhui Province, 230026, P. R. China

[b] iChEM (Collaborative Innovation Center of Chemistry for Energy Materials), University of Science and Technology of China, 96 Jin Zhai Rd, Hefei, Anhui Province, 230026, P. R. China

* Address correspondence to zhuyanwu@ustc.edu.cn

1　**Abstract:** Hematite (α-Fe$_2$O$_3$) nanoparticles are deposited onto a porous 'activated

2　microwave expanded graphite oxide' (aMEGO) carbon via a simple, rapid one-pot microwave

3　process. Under the irradiation of visible light, the α-Fe$_2$O$_3$/aMEGO composites exhibit

4　significantly enhanced photocatalytic activity for reduction Cr(VI) to Cr(III). A maximum

5　Cr(VI) removal rate of 95.28 % is obtained for the composite containing 7.72 wt.% aMEGO

6　as compared to that of 25.26 % for pure α-Fe$_2$O$_3$; the rate constant of the composite is nearly

7　9-fold higher than that of pure α-Fe$_2$O$_3$. The crucial role of aMEGO in enhancing the

8　photocatalytic efficiency of the composites relies not only on its large surface area, also on the

9　high conductivity which benefits to transport of photoexcited electrons. The enhancement in

10　charge separation and the suppression in electron-hole pair recombination is evidenced by

11　increased photocurrent and suppressed photoluminescence in α-Fe$_2$O$_3$/aMEGO composites.

12 **Keywords:** hematite, activated graphene, microwave-assisted, photocatalytic activity, Cr(VI)

13 reduction

14 **Introduction**

15 Unlike most organic pollutants, heavy metal contaminants are specially dangerous and

16 bothersome because they are unbiodegradable and apt to accumulate in living tissues

17 throughout the food chain.[1] In particular, hexavalent chromium (Cr(VI)) is a contaminant

18 frequently found in wastewater from industrial processes such as electroplating, metal

19 finishing, leather tanning, paint making, textile production and dyeing, etc.[2] Due to its high

20 toxicity, mutagenic and carcinogenic activity to human beings, and extremely high solubility

21 and mobility in water, Cr(VI) has been listed as one of primary pollutants by the United States

22 Environmental Protection Agency; its allowable content in drinking water has been strictly

23 regulated as 0.05 mg/L by The World Health Organization.[3] Hence, how to efficiently while

24 economically treat Cr(VI)-containing water has been a challenging topic for both academia

25 and industry. Various techniques such as chemical precipitation,[4] reverse osmosis,[5] ion

26 exchange,[6] foam flotation,[7] electrolysis,[8] adsorption[9] and photocatalytic reduction[3,10] have

27 been investigated for the Cr(VI) removal. Among these methods, photocatalytic reduction can

28 efficiently convert Cr(VI) to Cr(III), which is considered as a nontoxic and essential trace

29 metal in human nutrition within a certain limit,[10] and can be readily precipitated as $Cr(OH)_3$ in

30 neutral or alkaline solutions for the following removal as a solid waste.[3]

31 A broad range of semiconductors such as TiO_2, ZnO, CdS, SnS_2, In_2S_3 and so on have

32 been developed as photocatalysts to reduce Cr(VI) to Cr(III).[2,3,10-14] On the other hand, the

33 cost-effective, chemically stable and environmentally benign features make α-Fe_2O_3 a

34   promising candidate for an efficient photocatalyst.[15,16] α-Fe$_2$O$_3$ has a narrow bandgap (1.9-2.2

35   eV) which can be utilized to absorb visible light, a substantial fraction of the solar spectrum.

36   The poor conductivity and the short-hole diffusion length, however, has resulted in a quick

37   recombination of photo-induced electron-hole pairs in α-Fe$_2$O$_3$ and thus restricted its practical

38   applications in photocatalysis.[17-20] A variety of studies have been attempted to overcome these

39   obstacles, utilizing strategies such as metal,[21,22] non-metal doping[23,24] or carbon quantum dots

40   compositing.[25] To our best knowledge, there has no report published on α-Fe$_2$O$_3$ composites

41   for reducing Cr(VI).

42   Carbon is more chemically stable than metals and potentially has a high ion

43   adsorption efficiency. As a two dimensional (2D) allotrope of carbon with potentially high

44   carrier mobility,[26] graphene has been combined with α-Fe$_2$O$_3$, e.g. by hydrothermal

45   methods,[17,18] to form hybrid materials for improved photocatalytic performance in treating

46   organic pollutants. Pradhan et $al.$[18] reported a synthesis of α-Fe$_2$O$_3$ nanorod/reduced graphene

47   oxide (RGO) composites which showed a 4-fold enhancement compared with pure α-Fe$_2$O$_3$

48   nanorods in photodegradation efficiency for phenol. Han et $al.$[17] reported α-Fe$_2$O$_3$

49   nanoplate/RGO composites, based on which the rate constant is also four times higher than

50   that of pure α-Fe$_2$O$_3$ nanoplates for degradation of Rhodamine B (RhB). These efforts

51   suggested that α-Fe$_2$O$_3$/graphene composites have the potential to significantly enhance

52   photocatalytic activity for degradation of organic pollutants. However, the time-consuming

53   synthesis, the poor conductivity due to incomplete reduction of GO and the difficulty in

54   recycling of photocatalysts, may restrict the applications of α-Fe$_2$O$_3$/RGO catalysts. In

55   addition, the restacking of RGO nanoplates derived from GO limits the adsorption of

56   pollutants and thus deteriorates the performance. Ideally, a three-dimension (3D) porous

57   graphene structure with both high surface area and high electrical conductivity may act as an

58   excellent support of photocatalysts, probably leading to desired photocatalytic efficiency and

59   recyclability for the reduction of ions like Cr(VI).

60   In our previous work[27] a porous carbon called 'activated microwave expanded graphite

61   oxide' (aMEGO) was reported to have large surface areas of up to 3100 m^2/g and a high

62   electrical conductivity. In the present work, α-Fe_2O_3/aMEGO composites were synthesized by

63   a simple and rapid microwave process. The effects of aMEGO content in the composite on

64   structure, morphology, optical properties, photocurrent and photocatalytic properties of

65   α-Fe_2O_3/aMEGO composites were systematically investigated. In particular, for an optimal

66   content of 7.72 wt.% aMEGO in the composite, the photodegradation rate constant for

67   reduction Cr(VI) to Cr(III) of the composites reaches 9-fold higher than that of pure α-Fe_2O_3.

68   With cost-effective synthesis, the current work provides a potentially useful strategy for other

69   semiconductor/aMEGO composites with superior photocatalytic activity.

70   **Experimental Section**

71   **Sample Preparation**

72   Synthesis of aMEGO was performed by following the method described in Ref 27. For

73   synthesis of α-Fe_2O_3/aMEGO composites, aMEGO powder was suspended into ultrapure

74   water (2 mg/ml) and ultrasonicated (250 W) for 1 hr. Then various amounts of iron (III)

75   nitrate nonahydrate ($Fe(NO_3)_3 \cdot 9H_2O$) was added to the suspension, and the mixture

76   suspension was stirred using vacuum impregnation for 3 hr. After being dried in a vacuum

77   oven at 60°C for 12 hr, the mixture was placed into a domestic microwave oven for exposure

78   to microwave. The exposure duration and microwave power were 180 s and 500 W,

79   respectively. The composites with aMEGO to α-Fe$_2$O$_3$ ratios of 2:98, 5:95, 8:92, 10:90

80   (calculated based on the amount of aMEGO and Fe(NO$_3$)$_3$·9H$_2$O added) were obtained and

81   labeled   as   α-Fe$_2$O$_3$/aMEGO-1,   α-Fe$_2$O$_3$/aMEGO-2,   α-Fe$_2$O$_3$/aMEGO-3   and

82   α-Fe$_2$O$_3$/aMEGO-4, respectively. For comparison, pure α-Fe$_2$O$_3$ was also obtained by a direct

83   microwave-assisted heating of Fe(NO$_3$)$_3$·9H$_2$O, the exposure duration and microwave power

84   were 180 s and 500 W, respectively. All the chemicals were purchased from Sigma and used

85   without further purification.

86   **Characterizations**

87   The morphology, structure and composition of the samples were characterized by

88   scanning electron microscopy (SEM, JSM-6700F), high-resolution transmission electron

89   microscopy (HRTEM, JEOL 2010), and X-ray diffraction spectroscopy (XRD, D/max-TTR

90   III) with Cu Kα radiation (V = 40 kV, I = 200 mA), respectively. The scanning rate in XRD

91   was 5° min^{-1} from 10° to 80° (2θ). Fourier transform infrared spectroscopy (FTIR, NICOLET

92   8700), Raman spectroscopy (Renishaw inVia Raman Micro-scope, 532 nm laser, 5 mW) and

93   X-ray photoelectron spectroscopy (XPS, ESCALAB 250) were performed to further

94   characterize the chemical components in the composites. Thermogravimetry (TG) analysis of

95   the samples was carried out in air using a TGA Q5000 with a heating rate of 5 °C/min. The

96   specific surface areas were measured by nitrogen adsorption-desorption using a TriStar II

97   3020M with the Brunauer-Emmett-Teller (BET) method.

98   The absorption and fluorescence spectra of the samples were taken at room temperature

99   with   a   UV-visible   spectrophotometer   (Shimadzu   Solid   3700   spectrometer)   and   a

100   photoluminescence (PL) spectrofluorometer (JY Fluorolog-3-Tou) with an excitation light at

101   350 nm, respectively. Equation $(ahv) = A (hv – E_g)^n$ was used to estimate the band gap energy

102   of all catalysts, where a, v, A, and E_g are the absorption coefficient, light frequency,

103   proportionality constant and band gap energy, respectively; n describes type of transition in a

104   semiconductor, that is $n = 1/2$ for direct transition and $n = 2$ for indirect transition.[18,28] The

105   value of n for all the synthesized samples in this work was taken as 1/2, since the direct

106   optical transition in α-Fe$_2$O$_3$/aMEGO composites is allowed.[18] Photocurrent measurements

107   were performed on a CHI 602E electrochemistry potentiostat in a standard three-electrode

108   configuration with a photocatalyst-coated ITO glass as the working electrode, an Ag/AgCl as

109   reference electrode, and a Pt plate as counter electrode. In photocurrent measurements light

110   irradiation was provided by a 300 W xenon lamp with a cutoff filter ($\lambda > 420$ nm). Sodium

111   sulfate (Na$_2$SO$_4$, 0.5 M) solution was used as the electrolyte. To do the photocurrent

112   measurements, 10 μL slurry, which was made by dispersing 10 mg α-Fe$_2$O$_3$ or

113   α-Fe$_2$O$_3$/aMEGO in 0.5 mL H$_2$O followed by sonication for 2 hr, was dip-coated on the ITO

114   working electrodes and dried at room temperature. The scan rate was 50 mV/s, and all the

115   potentials are presented relative to Ag/AgCl.

116   **Photocatalytic Evaluation**

117   The photocatalytic performance of α-Fe$_2$O$_3$ or α-Fe$_2$O$_3$/aMEGO was evaluated by

118   photocatalytic reduction of Cr(VI) under visible light irradiation. The catalyst sample was

119   dispersed in 50 ml Cr(VI) solutions (10 mg/l) prepared by dissolving K$_2$Cr$_2$O$_7$ in deionized

120   water to a catalyst concentration of 1 mg/ml. At pH=2, the mixed suspension was first

121   magnetically stirred in the dark for 30 min to reach the adsorption-desorption equilibrium.

122   After that, the mixed suspension was exposed to visible light produced by the 300 W xenon

123   lamp (λ > 420 nm) under continuous stirring. With certain time intervals, 4 ml of the mixed

124   suspensions was extracted and centrifuged to remove the extra photocatalyst. Then the Cr(VI)

125   content in the solution was determined colorimetrically at 540 nm using the

126   diphenylcarbazide (DPC) method.[10] The reduction ratio (R_r) of Cr(VI) was calculated from

127   the measured absorbance intensity after a certain duration of illumination with the following

128   expression:

129    $R_r = (A_0 - A_t)/A_0 \times 100\%$,

130   where A_0 and A_t are the absorbance intensities of the sample taken when being illuminated for

131   0 min (measured right after the adsorption in dark but before the illumination) and t min of

132   illumination, respectively.

133   **Results and Discussion**

134   Scheme 1 illustrates a possible structure of α-Fe_2O_3/aMEGO composite, in which

135   α-Fe_2O_3 nanoparticles are attached in the matrix of highly porous aMEGO, as verified below.

136   With extremely high specific surface areas of up to 3100 m^2/g and essentially 100 % sp^2

137   carbon, aMEGO is presumably considered as a continuous 3D network of highly curved

138   atom-thick carbons.[27] aMEGO has been used as an electrically conductive scaffold for hosting

139   MnO_2 for superior energy storage.[29] Under visible light irradiation, electrons in α-Fe_2O_3 are

140   excited and electron-hole pairs are generated. Cr(VI) is reduced to Cr(III) by photogenerated

141   electrons, while water molecules are oxidized by the holes to oxygen.[28,30-35] In addition, due

142   to the high porosity and large surface area of aMEGO, the composite could potentially offer

143   more adsorption sites active to reactants around α-Fe_2O_3 nanoparticles thus might enhance the

144   catalytic reaction. Meanwhile, the excellent conductivity of aMEGO allows more efficient

145   electron-hole separation and thus prolongs the lifetime of the charge carriers, further

146   promoting the photocatalytic activity.

147   The SEM and HRTEM images in Figures 1A and 1B show the typical morphology of

148   aMEGO and 3D distribution of meso- and micropores as reported.[27] Below

149   α-Fe$_2$O$_3$/aMEGO-3 will be discussed as a representative of the composites due to the

150   optimized photocatalytic performance. After rapid one-pot microwave reaction, it is clearly

151   observed that aMEGO has been densely and uniformly decorated with α-Fe$_2$O$_3$ spherical

152   nanoparticles as shown in SEM and TEM images in Figures 1C and 1D. The typical size of

153   the nanoparticles shown in Figure 1D is about 20 nm, bigger than the average pore size of

154   aMEGO,[27] suggesting that most nanoparticles observed here are attached to the surface of

155   aMEGO. It is worth noting that even after 30 min of sonication for the preparation of TEM

156   specimen, aMEGO is still a stable support for anchoring α-Fe$_2$O$_3$ nanoparticles, indicated by

157   the strong combination between aMEGO and α-Fe$_2$O$_3$.[17, 18] The actual content of aMEGO in

158   as-synthesized composites has been determined as 2.14, 6.38, 7.72 or 11.36 wt.% for

159   α-Fe$_2$O$_3$/aMEGO-1, α-Fe$_2$O$_3$/aMEGO-2, α-Fe$_2$O$_3$/aMEGO-3   or α-Fe$_2$O$_3$/aMEGO-4,

160   respectively, by thermogravimetry (TG) analysis (Figure S1). The difference in the aMGEO

161   content from the originally calculated ratios could be partially explained by the loss of

162   aMEGO in the process of microwave reaction. TEM images of α-Fe$_2$O$_3$/aMEGO-1,

163   α-Fe$_2$O$_3$/aMEGO-2 and α-Fe$_2$O$_3$/aMEGO-4 are displayed in Figure S2. For

164   α-Fe$_2$O$_3$/aMEGO-1 with a low content of aMEGO, the apparent aggregation of nanoparticles

165   is observed, while the distribution of α-Fe$_2$O$_3$ nanoparticles is sparser with the increase in

166   aMEGO content. The HRTEM image in Figure 1E indicates the crystalline nature of the

167   α-Fe_2O_3 nanoparticles in α-Fe_2O_3/aMEGO-3. The lattice fringes are clearly observed with

168   spacings of 0.25 nm and 0.27 nm, corresponding to the interspatial distance of (110) and (104)

169   planes of α-Fe_2O_3 and consistent with the selected area electron diffraction (SAED) pattern

170   (inset of Figure 1E). The X-ray diffraction (XRD) patterns shown in Figure 1F further

171   confirm that the single-crystal hematite structure (JCPDS card No. 33-0664) of all

172   α-Fe_2O_3/aMEGO composites with different amount of aMEGO. No typical diffraction peaks

173   of aMEGO were detected, probably due to the low amount of aMEGO in the composite and

174   the amorphous structure of aMEGO (Figure S3A), similar to other semiconductor/RGO

175   composites.[17,28,36]

176   Elemental compositions of α-Fe_2O_3/aMEGO composites were characterized using X-ray

177   photoelectron spectroscopy (XPS) analysis. The C 1s XPS spectrum (Figure 2A) reveals the

178   four components at 284.78, 286.21, 287.55 and 289.07 eV corresponding to C-C bond with

179   sp^2 orbital, C-O, C=O and COOH functional groups, respectively. The presence and locations

180   of these peaks are in good agreement with those of aMEGO (Figure S3B). The O 1s spectrum

181   is shown in Figure 2B. The broad peak between 528 eV and 535 eV could be deconvoluted

182   into four peaks: a Fe-O signal appears at 529.80 eV, whereas the other peaks result from

183   oxygen-containing groups in aMEGO (Figure S3C), such as C=O at 531.35 eV, C-O at 532.48

184   eV and C-OH at 533.37 eV.[25] The Fe 2p spectrum in Figure 2C can be fitted to two peaks at

185   711.11 and 724.60 eV corresponding to the $2p_{3/2}$ and$2p_{1/2}$ spin-orbital components (with a

186   spin energy separation of 13.49 eV due to the spin-orbit coupling), respectively. A clearly

187   distinguishable satellite peak located at 719 eV, approximately 8 eV higher than the main Fe

188     $2p_{3/2}$ peak of α-Fe_2O_3, does not overlap either the Fe $2p_{3/2}$ or Fe $2p_{1/2}$ peak.[25,37] It can be solely

189   attributed to the presence of Fe^{3+} ions of α-Fe_2O_3 and all these peaks confirm the presence of

190   hematite in the composites (compared with Figure S3D).

191   Fourier transform infrared (FT-IR) spectroscopy was used to compare the chemical

192   structure of the pure aMEGO and α-Fe_2O_3/aMEGO composites. As shown in Figure 3A, the

193   FT-IR spectrum of aMEGO exhibits a broad band over the range of 3100-3600 cm^{-1},

194   associated with the stretching modes of hydroxy (-OH) groups. Other bands at ~2945 cm^{-1},

195   ~1634 cm^{-1} and ~1095 cm^{-1} are assigned to sp^3 C-H stretching, aromatic C=C and C-O

196   stretching vibration of COOH groups.[17,25,38] In comparison, α-Fe_2O_3/aMEGO-3 shows nearly

197   the same characteristic peaks to aMEGO and the strong peaks at 570 cm^{-1} and 480 cm^{-1} are

198   attributed to Fe-O vibrations, in agreement with those observed for the hematite particles.[25,38]

199   These results suggest that the chemical environment in aMEGO remains unchanged while

200   α-Fe_2O_3 nanoparticles are incorporated with aMEGO. Raman spectrum of aMEGO in Figure

201   3B showed two characteristic peaks at 1339 and 1589 cm^{-1}, corresponding to the breathing

202   mode of κ-point phonons of A_{1g} symmetry associated with the disorder and defects in

203   graphene (D band) and the first-order scattering of the E_{2g} phonon of sp^2 carbon atoms of

204   graphene (G band), respectively.[17] In the Raman spectrum of α-Fe_2O_3/aMEGO-3, the peaks at

205   215, 283 and 398 cm^{-1} are identified as the $A_{1g}(1)$, $E_g(2)$ and $E_g(4)$ of hematite.[37] Compared

206   with G peak located at 1589 cm^{-1} in aMEGO, the G peak in α-Fe_2O_3/aMEGO-3 has shifted to

207   1603 cm^{-1}, due to the charge transfer from aMEGO to α-Fe_2O_3, as found in other graphene

208   based composites.[39,40] The D peak of aMEGO overlaps with the magnon scattering of α-Fe_2O_3

209   (Figure S4), which makes the possible shift hard to be distinguished.[39] The same I(D)/I(G)

210   intensity ratios for aMEGO (1.211) and $\alpha\text{-Fe}_2\text{O}_3$/aMEGO-3 (1.207) suggests that the

211   introduction of $\alpha\text{-Fe}_2\text{O}_3$ has no significant influence on the defects and disorders in aMEGO.

212   The photocatalytic properties of $\alpha\text{-Fe}_2\text{O}_3$/aMEGO composites were evaluated by the

213   reduction of Cr(VI) under visible light irradiation. To rule out the contribution by the physical

214   adsorption in aMEGO-contained composites, a 30 min dark stirring has been carried out to

215   reach the adsorption-desorption equilibrium, as shown in Figure S5. Figure 4A shows the

216   photocatalytic reduction of Cr(VI) by $\alpha\text{-Fe}_2\text{O}_3$/aMEGO-3 through the temporal evolution

217   spectra, from which we can clearly see the characteristic absorption peak at 540 nm decreases

218   in intensity as the time prolongs. The variation in the degree of Cr(VI) degradation (C/C_0,

219   where C_0 and C is the initial concentration after the dark adsorption and the residual

220   concentration at a certain reaction time) with irradiation duration is shown in Figure 4B. Pure

221   $\alpha\text{-Fe}_2\text{O}_3$ shows a Cr(VI) reduction ratio of about 25.26% after 160 min of continuous

222   irradiation. With introducing aMEGO, the reduction ratio of the composites has been greatly

223   enhanced to 95.28% for $\alpha\text{-Fe}_2\text{O}_3$/aMEGO-3, after 160 min of visible light illumination.

224   However, further increase in the aMEGO content, e.g. to 11.36 wt.% in $\alpha\text{-Fe}_2\text{O}_3$/aMEGO-4,

225   leads to a little decrease in the photocatalytic activity, as also observed in other graphene

226   based photocatalysts.[17,18,28] We also investigated the factors affecting the photocatalytic

227   activity which involve adsorption capacity of pores, the light absorption ability, the carrier

228   separation and recombination efficiency as stated hereinafter. On the other hand, the rate

229   constant k, a basic kinetic parameter reflecting the reaction rate of the photocatalytic process,

230   was calculated from the pseudo first order kinetic equation $ln(C_0/C) = kt$, where t is reaction

231   time.[17] From the curves of $ln(C_0/C)$ versus t displayed in Figure 4C, the highest value of $k =$

232 0.01829 min^{-1} is obtained from α-Fe$_2$O$_3$/aMEGO-3, nearly 9-fold higher than that of pure

233 α-Fe$_2$O$_3$. In comparison, α-Fe$_2$O$_3$/RGO composites showed only a 4-fold enhancement based

234 on pure α-Fe$_2$O$_3$ in degradation efficiency for phenol or RhB.[17,18] We have also compared the

235 Cr(VI) reduction efficiency of α-Fe$_2$O$_3$/aMEGO with those of other graphene-based

236 semiconductor photocatalysts obtained under the optimal conditions for each. As can be seen

237 from Table S1, α-Fe$_2$O$_3$/aMEGO-3 has demonstrated one of the best performance under

238 visible irradiation among various graphene-based photocatalytic composites in terms of Cr(VI)

239 reduction efficiency.

240 The stability of α-Fe$_2$O$_3$/aMEGO-3 was further investigated by performing recycling

241 tests under identical conditions. As shown in Figure 4D, the photocatalytic activity of

242 α-Fe$_2$O$_3$/aMEGO-3 slightly decreases from 95.28% for the first cycle to 93.25% or 93.02%

243 for the second or third circles, respectively. As shown in Figure S6, the XRD pattern and SEM

244 image of α-Fe$_2$O$_3$/aMEGO-3 after three cycles show that the catalyst maintains the structure

245 and morphology as before cycling. The results indicate that the α-Fe$_2$O$_3$/aMEGO composites

246 can be used as highly efficient and stable visible light photocatalysts for Cr(VI) reduction in

247 water.

248 To obtain the hints about the mechanisms for the superior performance of

249 α-Fe$_2$O$_3$/aMEGO composites, the effects of specific surface area has been investigated.

250 Brunauer-Emmett-Teller (BET) surface areas calculated from nitrogen adsorption-desorption

251 isotherms (Figure S7) of α-Fe$_2$O$_3$ and α-Fe$_2$O$_3$/aMEGO composites are shown in Figure 5A.

252 Clearly, the introduction of aMEGO increased the surface area from 14.79 m^2/g for α-Fe$_2$O$_3$ to

253 above 120.50 m^2/g for α-Fe$_2$O$_3$/aMEGO-3 and α-Fe$_2$O$_3$/aMEGO-4 samples. With high

254 specific surface areas and highly curved 3D carbon network, aMEGO is used here as a porous

255 carrier without catalytic capacity (Figure S8). The enhanced surface area of the

256 α-Fe_2O_3/aMEGO composites could offer more active adsorption sites to adsorb more reactant

257 around catalyst and thus speed up the catalytic reaction. In addition, the optical absorption

258 properties of the composite catalysts were investigated by UV-vis diffuse reflectance spectra

259 (DRS), as shown in Figure 5B. α-Fe_2O_3 shows an absorption band at 526 nm corresponding to

260 the $2(^6A_1) \rightarrow (^4T_1)$ ligand field transition of Fe^{3+},[18,28] while all the aMEGO-loaded

261 photocatalysts showed a larger absorption edge, which is caused by the blackbody property of

262 aMEGO. The band gap estimated from the plot of $(ahv)^n$ versus hv is shown in the inset of

263 Figure 5B. The band gap has been reduced by introducing aMEGO in the composite, possibly

264 leading to higher and wider adsorption to visible light.

265 On the other hand, the photoelectrochemical property of the photocatalysts was

266 investigated with photocurrent measurement, shown in Figure 5C. As can be seen, the

267 α-Fe_2O_3/aMEGO composite electrodes generate much higher currents than α-Fe_2O_3 electrode

268 under the same applied potential without light irradiation (Figure 5C, line a'-e'). All samples

269 show increased currents when light is on, and α-Fe_2O_3/aMEGO composites show higher

270 currents compared to α-Fe_2O_3 (Figure 5C, line a-e). The current is enhanced with the increase

271 in the content of aMEGO, except for α-Fe_2O_3/aMEGO-4. Figure 5D shows the time response

272 of photocurrent for the catalysts by switching visible light illumination on and off sequentially.

273 It can be seen that, α-Fe_2O_3/aMEGO-3 composite has the highest photocurrent transient

274 response among the five samples studied, suggesting the remarkably efficient separation of

275 charge carriers, which is in agreement with the highest photoactivity of α-Fe_2O_3/aMEGO-3

276   toward reduction of Cr(VI).

277   The separation of charge carrier was also investigated with photoluminescence (PL).

278   Since PL emission results from the radiative recombination of excited electrons and holes it

279   has been a widely-technique to study the charge carrier transfer process as well as the

280   recombination process of the electron-hole pairs in semiconductors.[17] As demonstrated in

281   other graphene-based photocatalysts, such as α-Fe$_2$O$_3$ nanoplate/RGO,[17] α-Fe$_2$O$_3$

282   nanorod/RGO,[18] and α-FeOOH nanorod/RGO,[28] etc., PL displays a significant weakening

283   after RGO is introduced. Similarly, Figure 5E shows that after aMEGO is combined with

284   α-Fe$_2$O$_3$, the PL intensity of the composites decreases rapidly. The PL quenching further

285   confirms the role of aMEGO in inhibiting electron-hole pair recombination, which is

286   considered to highly contribute to the outstanding photocatalytic performance of

287   α-Fe$_2$O$_3$/aMEGO composites. In Figure 5E, we find with the increase in the content of

288   aMEGO (from 2.14 wt.% in α-Fe$_2$O$_3$/aMEGO-1 to 7.72 wt.% in α-Fe$_2$O$_3$/aMEGO-3), the PL

289   intensity of the composites reduces gradually; while the PL intensity of the composites

290   remains almost same when aMEGO content further increases from 7.72 wt.% in

291   α-Fe$_2$O$_3$/aMEGO-3 to 11.36 wt.% in α-Fe$_2$O$_3$/aMEGO-4. This implies that the suppression

292   efficiencies of photogenerated electron-hole pair recombination in α-Fe$_2$O$_3$/aMEGO-3 and

293   α-Fe$_2$O$_3$/aMEGO-4 are almost same.

294   The results above have clearly shown that the synergistic effect of between aMEGO and

295   α-Fe$_2$O$_3$ leads to the best photocatalytic efficiency through balancing the contribution of photo

296   absorption, physical adsorption and charge separation, e.g. in α-Fe$_2$O$_3$/aMEGO-3. Such a

297   combined effect may also explain why further increase aMEGO content, e.g. in

298 α-Fe$_2$O$_3$/aMEGO-4, results in a little decrease in photocatalytic activity, as also observed in

299 other graphene based photocatalysts.[17, 18, 28]

Conclusions

301 In summary, highly active α-Fe$_2$O$_3$/aMEGO composites with tunable content of aMEGO

302 were prepared by a simple, rapid, one-pot microwave process. The introduction of aMEGO

303 has led to larger surface areas, enhanced light absorption and fast transfer of photoexcited

304 electrons and more efficient separation of photo-generated electron-hole pairs. As a

305 consequence, the α-Fe$_2$O$_3$/aMEGO-3 with optimal content of aMEGO achieves a high Cr(VI)

306 removal rate of 95.28% under visible light irradiation, compared to 25.26% of pure α-Fe$_2$O$_3$.

307 The rate constant has been enhanced for nearly 9-fold. The synergistic effects between

308 α-Fe$_2$O$_3$ and aMEGO may benefit to the development of low-cost, safe and green

309 α-Fe$_2$O$_3$/aMEGO composites potentially useful for treating wastewater.

Acknowledgements

Notes and References

315 1. C. E. Barrera-Díaz, V. Lugo-Lugo and B. Bilyeu, *J. Hazard. Mater.*, 2012, **223**, 1-12.

316 2. C. Mondal, M. Ganguly, J. Pal, A. Roy, J. Jana and T. Pal, *Langmuir*, 2014, **30**,

317 4157-4164.

318 3. Z. Jin, Y. X. Zhang, F. L. Meng, Y. Jia, T. Luo, X. Y. Yu, J. Wang, J. H. Liu and X. J.

319 Huang *J. Hazard. Mater.*, 2014, **276**, 400-407.

320   4. M. Gheju and I. Balcu, *J. Hazard. Mater.*, 2011, **196**, 131-138.

321   5. L. Cui, Q. Meng, J. Zheng, X. Wei and Z. Ye, *Vacuum*, 2013, **89**, 1-6.

322   6. Y. Deng, T. Long, H. Zhao, L. Zhu and J. Chen, *Sep. Sci. Technol.*, 2012, **47**, 256-263.

323   7. A. I. Zouboulis, N. K. Lazaridis and D. Zamboulis, *Sep. Sci. Technol.*, 1994, **29**, 385-400.

324   8. H. Sarahney, X. Mao and A. N. Alshawabkeh, *Electrochim. Acta.*, 2012, **86**, 96-101.

325   9. W. Li, Y. Tang, Y. Zeng, Z. Tong, D. Liang and W. Cui, *Chem. Eng. J.*, 2012, **193**, 88-95.

326   10. Y. C. Zhang, J. Li, M. Zhang and D. D. Dionysiou, *Environ. Sci. Technol.*, 2011, **45**,

327   9324-9331.

328   11. C. Wang, M. Cao, P. Wang, Y. Ao, J. Hou and J. Qian, *Appl. Catal., A*, 2014, **473**, 83-89.

329   12. X. Liu, L. Pan, Q. Zhao, T. Lv, G. Zhu, T. Chen, T. Lu, Z. Sun and C. Sun, *Chem. Eng.*

330   *J.*, 2012, **183**, 238-243.

331   13. X. Liu, L. Pan, T. Lv, G. Zhu, Z. Sun and C. Sun, *Chem. Commun.*, 2011, **47**,

332   11984-11986.

333   14. X. An, C. Y. Jimmy, F. Wang, C. Li and Y. Li, *Appl. Catal., B*, 2013, **129**, 80-88.

334   15. X. Zhou, J. Lan, G. Liu, K. Deng, Y. Yang, G. Nie, J. Yu and L. Zhi, *Angew. Chem. Int.*

335   *Ed.*, 2012, **124**, 182-186.

336   16. H. Liang, X. Xu, W. Chen, B. Xu and Z. Wang, *CrystEngComm*, 2014, **16**, 959-963.

337   17. S. Han, L. Hu, Z. Liang, S. Wageh, A. A. Al-Ghamdi, Y. Chen and X. Fang, *Adv. Funct.*

338   *Mater.*, 2014, **24**, 5719-5727.

339   18. G. K. Pradhan, D. K. Padhi and K. M. Parida, *ACS Appl. Mater. Interfaces*, 2013, **5**,

340   9101-9110.

341   19. C. Jorand Sartoretti, B. D. Alexander, R. Solarska, I. A. Rutkowska, J. Augustynski and R.

342   Cerny, *J. Phys. Chem. B*, 2005, **109**, 13685-13692.

343   20. M. Zhang, Y. Lin, T. J. Mullen, W. F. Lin, L. D. Sun, C. H. Yan, T. E. Patten, D. Wang and

344   G. Y. Liu, *J. Phys. Chem. Lett.*, 2012, **3**, 3188-3192.

345   21. W. Cheng, J. He, Z. Sun, Y. Peng, T. Yao, Q. Liu, Y. Jiang, F. Hu, Z. Xie and S. Wei, *J.*

346   *Phys. Chem. C*, 2012, **116**, 24060-24067.

347   22. A. J. Frierdich, M. M. Scherer, J. E. Bachman, M. H. Engelhard, B. W. Rapponotti and J.

348   G. Catalano, *Environ. Sci. Technol.*, 2012, **46**, 10031-10039.

349   23. T. H. Jeon, W. Choi and H. Park, *J. Phys. Chem. C*, 2011, **115**, 7134-7142.

350   24. W. Yan, H. Fan and C. Yang, *Materials Letters*, 2011, **65**, 1595-1597.

351   25. B. Y. Yu and S. Y. Kwak, *J. Mater. Chem.*, 2012, **22**, 8345-8353.

352   26. K. S. Novoselov, A. K. Geim, S. V.bMorozov, D. Jiang, Y. Zhang, S. V. Dubonos, I. V.

353   Grigorieva and A. A. Firsov, *Science*, 2004, **306**, 666-669.

354   27. Y. Zhu, S. Murali, M. D. Stoller, K. J. Ganesh, W. Cai, P. J. Ferreira, A. Pirkle, R. M.

355   Wallace, K. A. Cychosz, M. Thommes, D. Su, E. A. Stach and R. S. Ruoff, *Science*, 2011,

356   **332**, 1537-1541.

357   28. D. K. Padhi and K. Parida, *J. Mater. Chem. A*, 2014, **2**, 10300-10312.

358   29. X. Zhao, L. Zhang, S. Murali, M. D. Stoller, Q. Zhang, Y. Zhu and R. S. Ruoff, *ACS nano*,

359   2012, **6**, 5404-5412.

360   30. F. Meng, J. Li, S. K. Cushing, J. Bright, M. Zhi, J. D. Rowley, Z. Hong, A. Manivannan, A.

361   D. Bristow and N. Wu, *ACS Catal.*, 2013, **3**, 746-751.

362   31. Q. L. Yang, S. Z. Kang, H. Chen, W. Bu and J. Mu, *Desalination*, 2011, **266**, 149-153.

363   32. R. Mu, Z. Xu, L. Li, Y. Shao, H. Wan and S. Zheng, *J. Hazard. Mater.*, 2010, **176**,

364   495-502.

365   33. A. Idris, N. Hassan, N. S. M. Ismail, E. Misran, N. M. Yusof, A. F. Ngomsik and A. Bee,

366   *Water Res.*, 2010, **44**, 1683-1688.

367   34. T. Papadam, N. P. Xekoukoulotakis, I. Poulios and D. Mantzavinos, *J. Photoch. Photobio.*

368   *A*, 2007, **186**, 308-315.

369   35. S. Tuprakay and W. Liengcharernsit, *J. Hazard. Mater.*, 2005, **124**, 53-58.

370   36. Z. Yan, X. Yu, A. Han, P. Xu and P. Du, *J. Phys. Chem. C*, 2014, **118**, 22896-22903.

371   37. B. Ahmmad, K. Leonard, M. Shariful Islam, J. Kurawaki, M. Muruganandham, T. Ohkubo

372   and Y. Kuroda, *Adv. Powder. Technol.*, 2013, **24**, 160-167.

373   38. X. Li, X. Yu, J. He and Z. Xu, *J. Phys. Chem. C*, 2009, **113**, 2837-2845.

374   39. J. Qu, Y. X. Yin, Y. Q. Wang, Y. Yan, Y. G. Guo and W. G. Song, *ACS Appl. Mater.*

375   *Interfaces*, 2013, **5**, 3932-3936.

376   40. J. Liu, H. Cao, J. Xiong and Z. Cheng, *CrystEngComm*, 2012, **14**, 5140-5144.
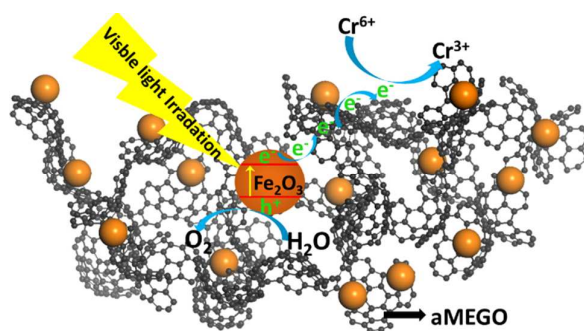
Scheme 1. Schematic illustration for the photocatalytic reduction of Cr(VI) with α-Fe_2O_3/aMEGO composites under visible light irradiation.
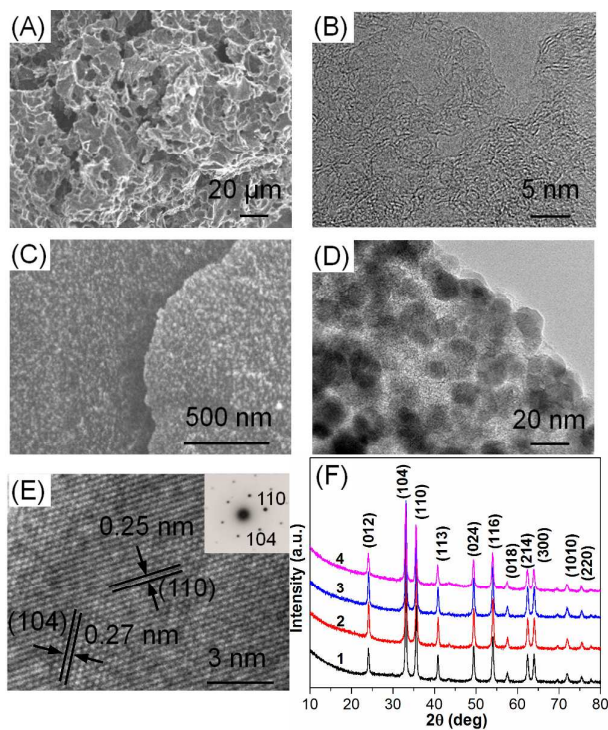
Figure 1. (A) SEM and (B) TEM images of aMEGO; (C) SEM and (D) TEM images of α-Fe$_2$O$_3$/aMEGO-3; (E) HRTEM image of α-Fe$_2$O$_3$/aMEGO-3. The inset is the corresponding SAED pattern of α-Fe$_2$O$_3$ nanoparticles; (F) XRD patterns of the α-Fe$_2$O$_3$/aMEGO-1 (curve1), α-Fe$_2$O$_3$/aMEGO-2 (curve2), α-Fe$_2$O$_3$/aMEGO-3 (curve3) and α-Fe$_2$O$_3$/aMEGO-4 (curve4).
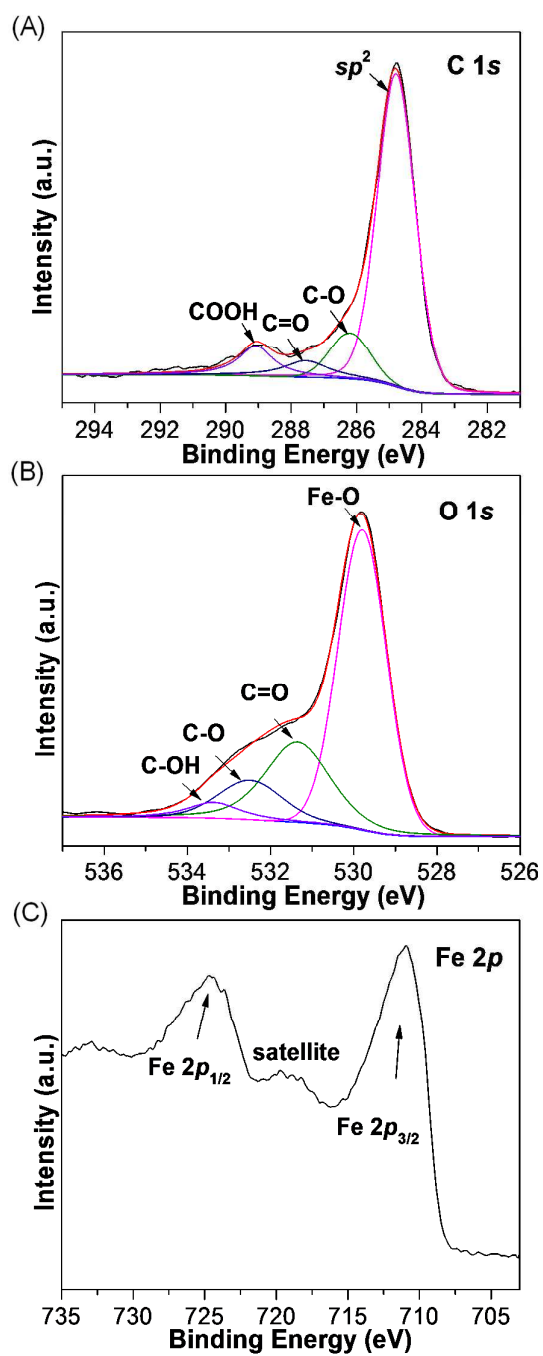
Figure 2. XPS spectra of α-Fe$_2$O$_3$/aMEGO-3: (A) C 1s spectrum, (B) O 1s spectrum and (C)
Fe 2p spectrum.
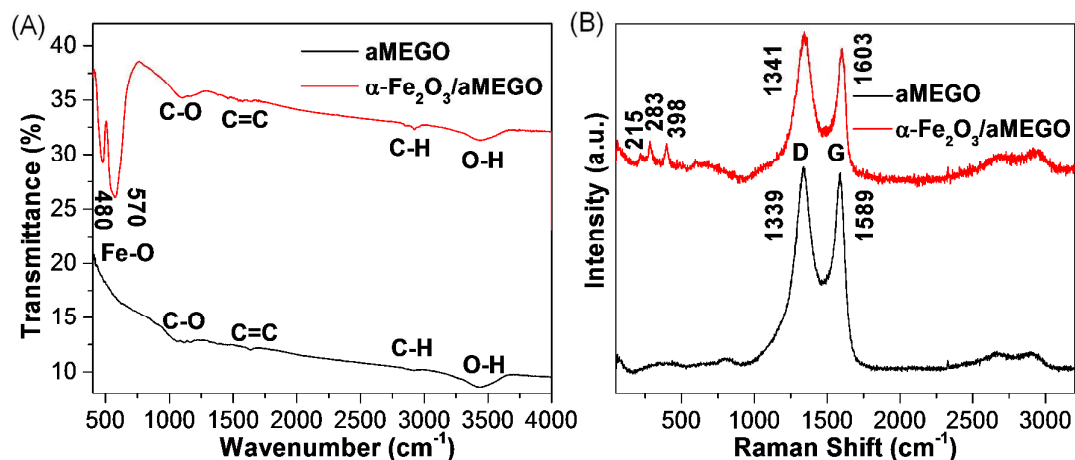
Figure 3. FT-IR spectra (A) and Raman spectra (B) of aMEGO and α-Fe$_2$O$_3$/aMEGO-3.
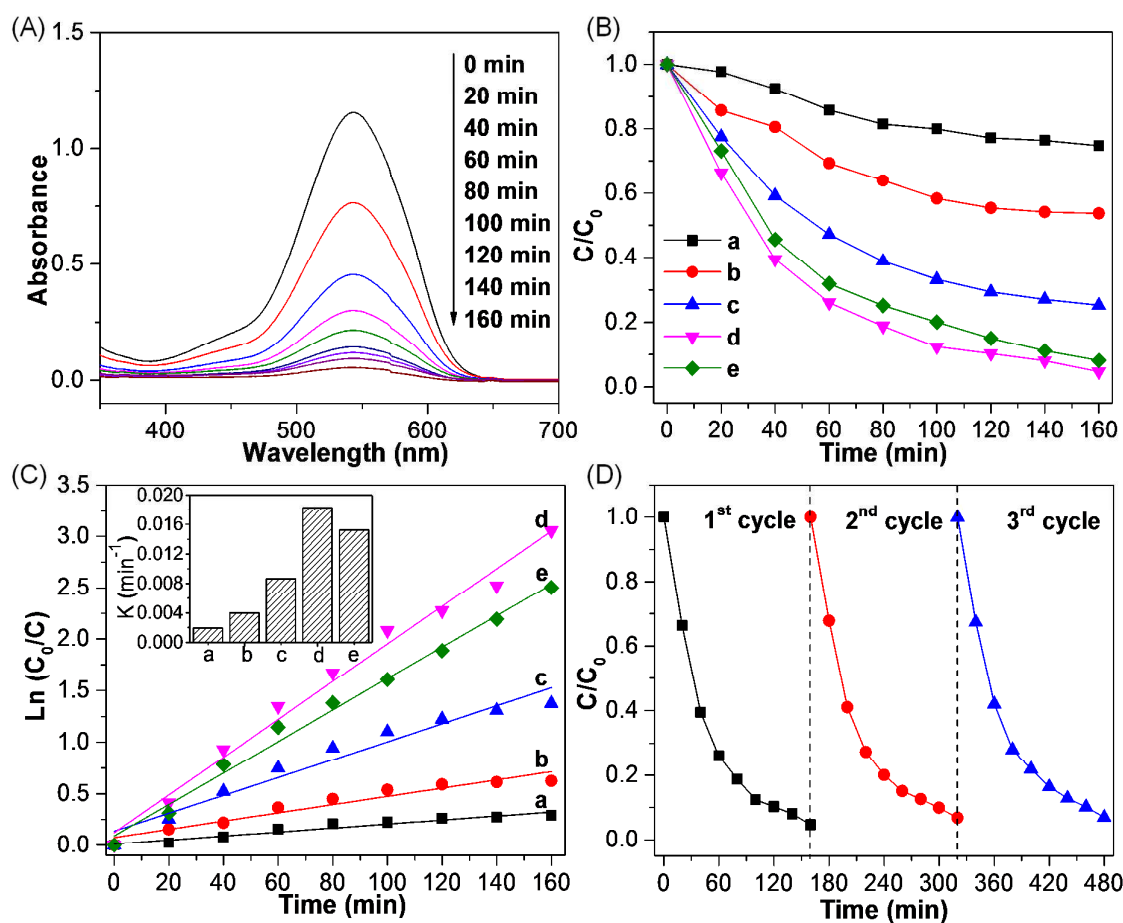
Figure 4. (A) Time-dependent UV-vis absorption spectra of DPC-Cr(VI) complex solutions in the presence of α-Fe$_2$O$_3$/aMEGO-3 under visible light irradiation. (B) Photocatalytic reduction of aqueous Cr(VI) and (C) Kinetic curves of the degradation process by (a) α-Fe$_2$O$_3$, (b) α-Fe$_2$O$_3$/aMEGO-1, (c) α-Fe$_2$O$_3$/aMEGO-2, (d) α-Fe$_2$O$_3$/aMEGO-3 and (e) α-Fe$_2$O$_3$/aMEGO-4 under visible light irradiation. The inset of (C) is the corresponding rate

constant. (D) Cyclic photocatalytic reduction of aqueous Cr(VI) by α-Fe$_2$O$_3$/aMEGO-3.
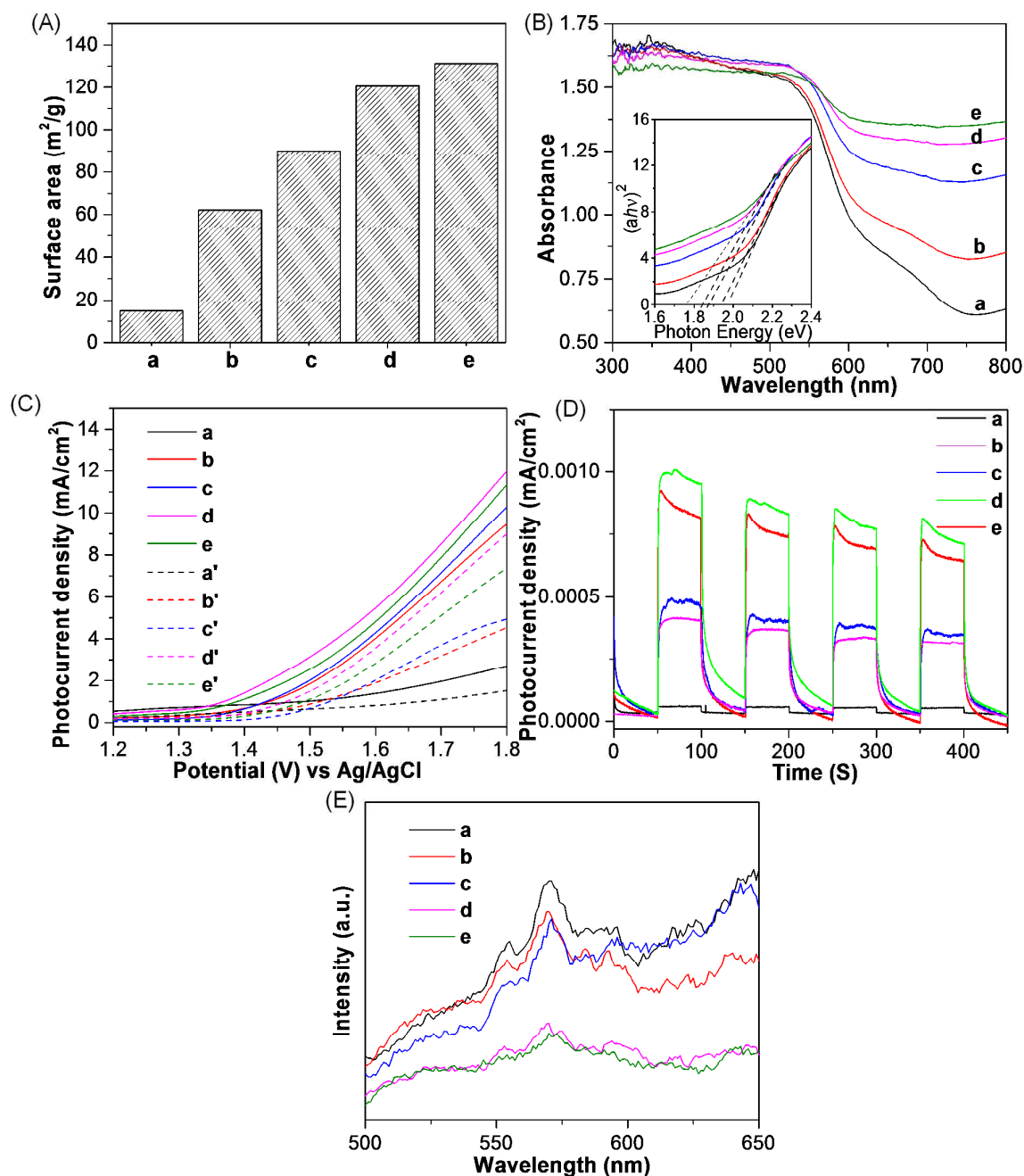
Figure 5. (A) Surface area and (B) UV-vis absorption spectra for α-Fe$_2$O$_3$ and α-Fe$_2$O$_3$/aMEGO composites. The inset is corresponding Tauc plot analysis of optical band gap of direct transition. (C) Linear sweep voltammagrams with (a-e) and without (a'-e') visible light irradiation. (D) Amperometric I-t curves with an electrode potential of 0.6 V versus Ag/AgCl with 50 s visible light on/off cycles. (E) PL spectra. In all figures a: α-Fe$_2$O$_3$, b: α-Fe$_2$O$_3$/aMEGO-1, c: α-Fe$_2$O$_3$/aMEGO-2, d: α-Fe$_2$O$_3$/aMEGO-3 and e:

α-Fe$_2$O$_3$/aMEGO-4.

Table of Contents

α-Fe$_2$O$_3$/aMEGO composites are demonstrated to be excellent photocatalysts in Cr(VI) reduction.